Geometry and Segmentation of Cerberus Fossae, Mars: Implications for Marsquake Properties

C. Perrin[1,2] , A. Jacob[1] , A. Lucas[1] , R. Myhill[3] , E. Hauber[4] , A. Batov[5,6] , T. Gudkova[5] , S. Rodriguez[1] , P. Lognonné[1] , J. Stevanović[7] , M. Drilleau[8] , and N. Fuji[1]

[1]Université de Paris, Institut de physique du globe de Paris, CNRS, Paris, France, [2]Now at Nantes Université, Université d'Angers, Le Mans Université, CNRS, UMR 6112, Laboratoire de Planétologie et Géosciences, UAR 3281, Observatoire des Sciences de l'Univers de Nantes Atlantique, Nantes, France, [3]School of Earth Sciences, University of Bristol, Bristol, UK, [4]DLR Institute of Planetary Research, Berlin, Germany, [5]Schmidt Institute of Physics of the Earth, Russian Academy of Sciences, Moscow, Russia, [6]V.A. Trapeznikov Institute of Control Sciences, Russian Academy of Sciences, Moscow, Russia, [7]AWE Blacknest, Reading, UK, [8]Institut Supérieur de l'Aéronautique et de l'Espace ISAE-SUPAERO, Toulouse, France

Abstract The NASA InSight mission to Mars successfully landed on 26 November 2018 in Elysium Planitia. It aims to characterize the seismic activity and aid in the understanding of the internal structure of Mars. We focus on the Cerberus Fossae region, a giant fracture network ∼1,200 km long situated east of the InSight landing site where M ∼3 marsquakes were detected during the past 2 years. It is formed of five main fossae located on the southeast of the Elysium Mons volcanic rise. We perform a detailed mapping of the entire system based on high-resolution satellite images and Digital Elevation Models. The refined cartography reveals a range of morphologies associated with dike activity at depth. Width and throw measurements of the fossae are linearly correlated, suggesting a possible tectonic control on the shapes of the fossae. Widths and throws decrease toward the east, indicating the long-term direction of propagation of the dike-induced graben system. They also give insights into the geometry at depth and how the possible faults and fractures are rooted in the crust. The exceptional preservation of the fossae allows us to detect up to four scales of segmentation, each formed by a similar number of 3–4 segments/subsegments. This generic distribution is comparable to continental faults and fractures on Earth. We anticipate higher stress and potential marsquakes within intersegment zones and at graben tips.

Plain Language Summary The landing of the InSight mission on Mars and the deployment of its seismometer have renewed the interest of active Martian structures that could trigger seismic events. In this study, we focus on one of these structures, Cerberus Fossae, which is a large fracture network situated close to the landing site. We perform a detailed mapping of the fossae based on high-resolution satellite images and present an analysis of their lateral segmentation and morphology. We assess an eastward direction of long-term propagation of the fossae. We also find that the fossae are laterally segmented at four different scales: fossae are divided into major segments, which are themselves divided into secondary segments and so on. At each scale of segmentation, a similar number of three to four subsegments is found. This number is also observed along terrestrial fault systems. These results allow us to assess the overall and local stress concentrations along the fossae: we infer that those stresses are higher eastward near the tip of the fossae and at intersegment zones. Since marsquakes are difficult to locate precisely with a single seismic station, our study is an asset to reduce uncertainties and to better understand the source properties.

1. Introduction

Launched on 5 May 2018 and successfully landed on Elysium Planum on 26 November 2018, the NASA's Discovery Interior Exploration using Seismic Investigations, Geodesy and Heat Transport (InSight) mission is dedicated to the study of the Martian interior (Banerdt et al., 2020). The main instrument, the Seismic Experiment for Interior Structure (SEIS; Lognonné et al., 2019) seismometer, is designed to record Martian seismic activity from different seismic sources: atmospheric turbulence (Spiga et al., 2018), airbursts and meteorite impacts (Daubar et al., 2018; Stevanović et al., 2017), and internal seismic activity of the planet (Clinton et al., 2018). In this study, we focus on the potential seismic activity of major tectonic structures close to the landing site (Golombek et al., 2020).
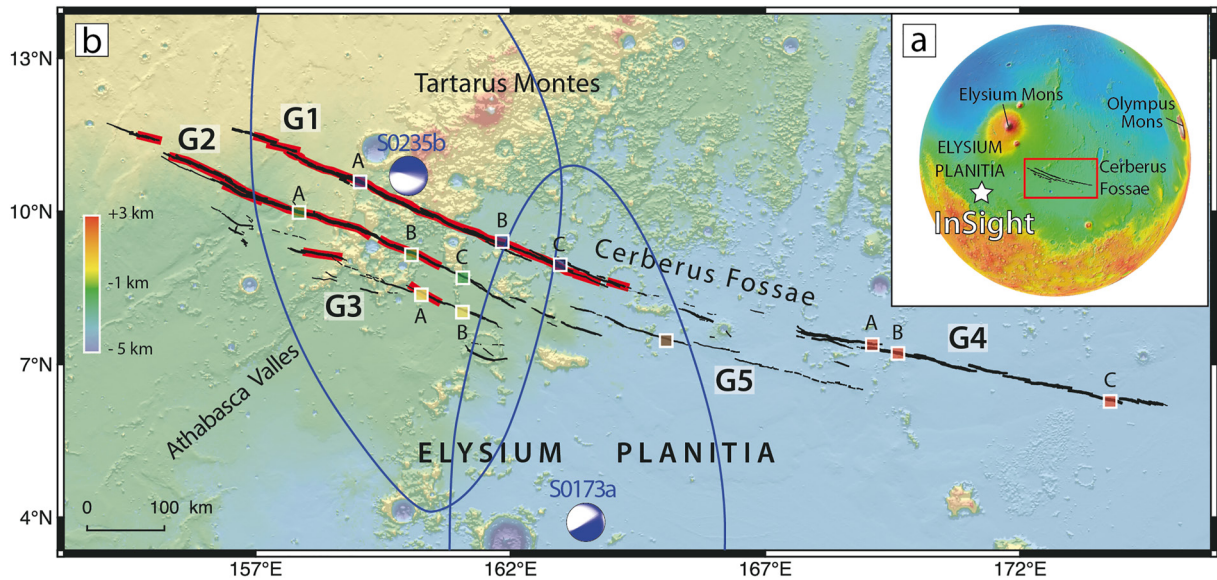
Figure 1. (a) Topographic map of Mars (MOLA; Smith et al., 2001). The InSight landing site is indicated by the white star. The area of interest is included in the red rectangle. (b) Tectonic fault map focusing on Cerberus Fossae. Red lines are low-resolution surface traces mapped by Knapmeyer et al. (2006). Black lines are surface traces from this study. Colored rectangles on each fossa point out HiRISE stereo pairs images used in this study (Figure 5). G1–G5 indicate the five major subparallel fossae (modified from Taylor et al., 2013). The blue ellipsoids and focal mechanisms of events S0173a and S0235b are modified from Giardini et al. (2020) and Brinkman et al. (2021), respectively.

Situated ~1,200 km to the northeast of the landing site, the giant fracture set of Cerberus Fossae is one of the closest major visible structures (Figure 1a) that could generate marsquakes recordable by the SEIS seismometer. Before the InSight mission, Taylor et al. (2013) considered Cerberus Fossae as an active seismic source with an estimated seismic moment release of the order of 10^{17} N·m·yr^{-1}. Since the InSight landing, SEIS has recorded several hundreds of events (Ceylan et al., 2021; Clinton et al., 2021; Giardini et al., 2020; Lognonné et al., 2020), but only ~10% of them are clearly identified as marsquakes. Furthermore, the difficulty to observe clear seismic phase arrivals and polarizations on seismic records allowed Giardini et al. (2020) to determine the location of only two main events (M ~3 S0173a and S0235b events). Despite the large uncertainties, both events were located within the Cerberus Fossae region (Figure 1b). This first striking observation was associated with the study of Brinkman et al. (2021), who have shown that extensional dip-slip motion occurred during these marsquakes (Figure 1b), raising the possibility of ongoing and localized tectonic activity on Mars.

In order to better locate and determine the magnitude of such marsquakes originating from this major system, it is important to characterize in detail its surface trace and its along-strike structural discontinuities (i.e., step overs, bends, secondary faults, and fractures). Lateral fault and fracture segmentation is an important property that has a strong impact on rupture initiation, propagation, and arrest (e.g., Aki, 1979; Barka & Kadinsky-Cade, 1988; Biasi & Wesnousky, 2016, 2017; Manighetti et al., 2007, 2015; Shaw, 2006; Sibson, 1986; Zhang et al., 1999). In this study, we use high-resolution satellite images (Martian Reconnaissance Orbiter's Context Camera CTX with a horizontal spatial sampling of 6 m/pixel; Malin et al. (2007); High-Resolution Imaging Science Experiment [HiRISE] with a horizontal spatial sampling of 25 cm/pixel; McEwen et al. (2007)) to map in detail the entire Cerberus Fossae system. We build Digital Elevation Models (DEMs) from stereo pair images in order to study the detailed morphology of the fossae. We analyze the lateral segmentation of the fossae and highlight several scales of segmentation. We do not aim to prove the existence of dikes at depth but rather discuss the growth process and the direction of long-term propagation of the whole system. Finally, we discuss the preferential location of seismic events deduced from our analysis to help to better locate the events recorded by InSight.

2. General Context of Cerberus Fossae

The Cerberus Fossae crosscut one of the youngest Martian volcanic terrains dated to Late Amazonian (1 Gyr to present; Plescia, 1990, 2003; Tanaka et al., 1992). It is located in the Elysium Planitia, near Elysium Mons (Figure 1a) and is ~1,200 km long (coordinates between 6°–12°N and 157°–174°E). It is formed by 4–5 major sub-parallel fossae (long linear and narrow depressions on Mars, labeled G1 to G5 on Figure 1b; modified from Taylor et al., 2013), ranging from ~250 to ~600 km long, and trending N110°E in the northwest part (western fossae) to N100°E in the southeast (eastern fossae). From orbit, fossae appear as giant fractures that Ernst et al. (2002) identified as the result of possible giant dike swarms at depth, radiating from Elysium Mons. Using a flexural loading model, Hall et al. (1986) showed that the global stress field induced by the Tharsis rise might also be responsible for the formation of the fossae. It is thought that the fossae formed in a regional extensional stress setting either due to pure graben faulting (Vetterlein & Roberts, 2010) or fracturing processes above growing dike(s) at depth (e.g., Berman & Hartmann, 2002; Burr et al., 2002; Head et al., 2003; Nahm et al., 2015, 2016; Plescia, 1990) as commonly observed on Earth (e.g., Gudmundsson, 1984; Hjartardóttir et al., 2016; Magee & Jackson, 2021; Rowland et al., 2007; Rubin, 1992; Rubin & Pollard, 1988; Tentler, 2005). Many studies have also pointed out the local influence of the combined effect of dike intrusion and subsurface cryospheric melting, which led to large lava flows and catastrophic floods of melt water at the surface of Mars that shaped the surrounding plains of the near-fossae regions (e.g., Burr et al., 2002; Cassanelli & Head, 2018; Nahm et al., 2015, 2016; Pendleton, 2015; Plescia, 2003).

Taylor et al. (2013) have inferred that Cerberus Fossae might be an active tectonic structure, which are able to release a seismic moment of 10^{15}–10^{17} Nm·yr^{-1}. They associated this late tectonic activity (i.e., <10 Myr) with recent volcanism evidenced by young lava flows (Vaucher et al., 2009). Recently, Horvath et al. (2021) even identified *a* <250 ka old pyroclastic volcanic deposit in the central part of the fossae, supporting the hypothesis that geological activity continues to present day. Since 2018, the InSight mission has confirmed that multiple seismic events (or marsquakes) of M ~3.5 originated in the vicinity of Cerberus Fossae (e.g., Giardini et al., 2020) in good agreement with pre-mission estimations (Böse et al., 2017; Panning et al., 2017). The moderate-sized magnitudes are supposedly too low to trigger surface ruptures. Recently, Grindrod et al. (2018) reported locally no coseismic deformations at a single location along fossae G2 by performing sub-pixel correlation analysis (i.e., COSI-Corr; Leprince et al., 2007) on HiRISE images over a period of 8 years. However, Roberts et al. (2012) studied the potential paleo-marsquakes that occurred along fossae G2 by analyzing along-strike distributions of boulders triggered by ground shaking. They found a dense distribution of boulders over a distance of 90–150 km, which could have originated from a sequence of several large paleo-marsquakes that might have caused surface ruptures in the last 2.5 Ma (see also Section 4.2.2).

3. Data Analysis and Results

3.1. Detailed Mapping of Cerberus Fossae

Available geological and fault maps of Mars highlight the major structures composing the Martian crust (e.g., Knapmeyer et al., 2006; Tanaka et al., 1992). However, they are mainly based on low-resolution satellite observations (e.g., MOLA, the only data set available at that time and covering the entire planet), which are not of sufficient resolution to depict geological structures at a smaller scale (average horizontal spatial sampling of 463 m/pixel; Smith et al., 2001). Here, we used high-resolution satellite images (6 m/pixel CTX and 25 cm/pixel HiRISE images) to perform a detailed mapping of the entire Cerberus Fossae system. The resolution of these images made it possible to identify a large amount of new fossae (black lines, Figure 1b) that were not mapped by Knapmeyer et al. (2006) (red lines, Figure 1b). For example, fossae G1 and G2 are visible on MOLA data, while smaller fossae G3, G4, and G5 are not. Still, the latter fossae were observed in previous studies (e.g., Berman & Hartmann, 2002; Grindrod et al., 2018; Plescia, 1990; Taylor et al., 2013) based on medium- to high-resolution satellite images (Viking, THEMIS, HRSC, CTX, and HiRISE). G4 may be the eastern extension of G1, but there is no clear evidence of continuous surface expression between them (the gap is more than 100 km long). Most of the mapped traces are clearly expressed at the ground surface (G1, G2, and G4; Figures 1, 2a, 2b and 2c), while some of them are less distinct, especially along G3 and G5, where shallow traces (Figure 2d), narrow fractures (Figure 2e), and discontinuous traces (Figure 2f) are observed, possibly related to early collapse of a putative lava conduit or melting and consequent collapse of the cryosphere at depth. The length of the fossae ranges from 260
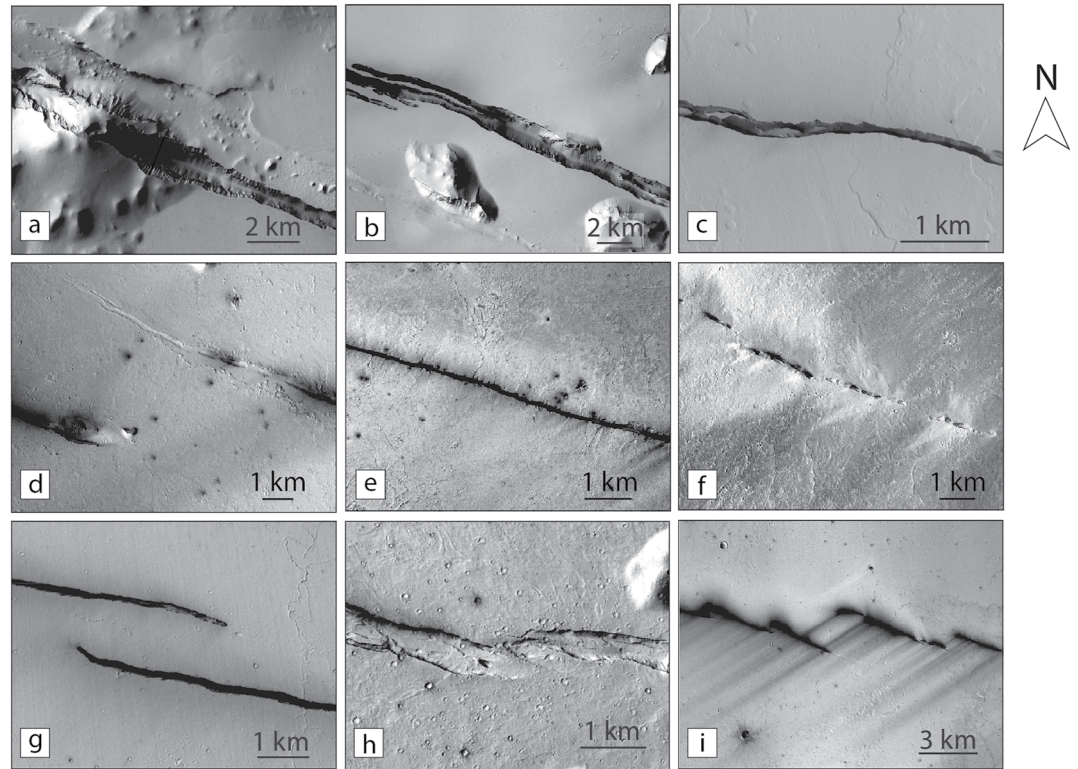
Figure 2. CTX images of the Cerberus Fossae surface traces, from clear and large fossae along (a and b) G1 and (c) G4 to (d) shallow, (e) narrow, and (f) discontinuous traces along G3, G2, and G5, respectively. (g, h, i) Examples of relay zones between segments at different scales along G4.

to 610 km. Their traces are subparallel and spaced from 20 to 60 km apart (G1, G2, G3, and G5). Vetterlein and Roberts (2010) measured the height of the walls of the fossae and found a maximum vertical height of ~1 km (i.e., summed walls are 2 km high in the case of a symmetric fossa) in the western part of G1, which is the closest section of the Cerberus Fossae system to Elysium Mons.

3.2. Lateral Segmentation of Cerberus Fossae

All faults and fractures are structurally segmented along their trace, regardless of their scale, slip mode, or tectonic context. The segments constitute small subparallel delineations on the fault strike, separated by jumps corresponding to zones of slip deficit and hence stress concentrations (e.g., Barka & Kadinsky-Cade, 1988; Klinger, 2010; Manighetti et al., 2015; Segall & Pollard, 1980). Moreover, Manighetti et al. (2015) have shown that faults on Earth are segmented at hierarchical scales, that is, faults are divided into three to four major segments, themselves divided into two to three secondary segments. Previous studies have already shown that faults on Mars are laterally segmented (e.g., Donzé et al., 2021; Hauber et al., 2014; Polit et al., 2009; Schultz, 1989), and the fossae of Cerberus are no exception (Vetterlein & Roberts, 2010). They are formed by numerous segments at different scales, separated by various structural discontinuities, such as step overs (Figure 2g), complex relay zones (Figure 2h), and en échelon structures (Figure 2i).

We analyzed the lateral segmentation of the Cerberus Fossae system based on our complete surface mapping (Figure 3, Figure S1 in Supporting Information S1). Due to the very low erosion rate on Mars, segments are well preserved. They are well connected in the western and northern parts of the fossae system (G1 and G2; Figure S1 in Supporting Information S1), whereas they are rather isolated and offset in the eastern and southern parts (G3, G4, and G5). We are able to identify up to four scales of segmentation on G2 and G4 and three scales on G1 and G3 (see detail in Figure 3 and Figure S1 in Supporting Information S1). Note that we do not describe G5's segmentation in this section since its trace is too discontinuous. Note also that our definitions of segments of G1
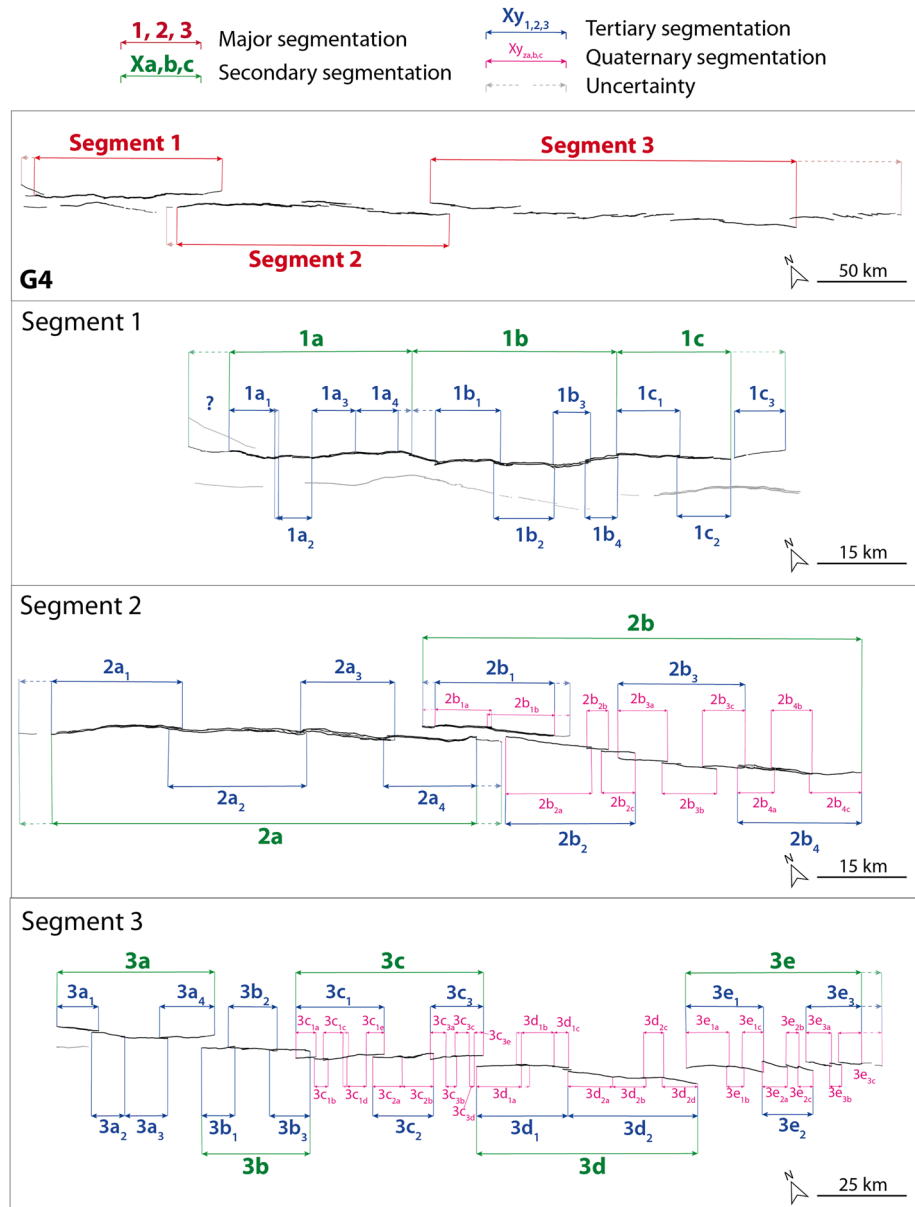
Figure 3. Representation of the four scales of segmentation analyzed in this study. Black lines are traces of fossa G4 of Cerberus Fossae in map view (see other fossae in Figure S1 in Supporting Information S1). A closer view of the subsegments in each major segment is shown. A detailed description of the segmentation is available in Text S1 in Supporting Information S1.

are slightly different from those defined by Vetterlein and Roberts (2010). We justify our choices in the discussion (see Section 4.2.1).

As an example, we give below a detailed description of G4's lateral segmentation (Figure 3), a fossa not extensively described in the literature compared to other western fossae in Cerberus. The detailed description of the segmentation of the entire Cerberus Fossae system can be found in Figure S1 and Text S1 in Supporting Information S1. We define major segments as those separated by the largest structural discontinuities found, such as large step overs, and/or secondary splay faults, and/or major bends along the surface traces. These zones also appear as the largest slip deficit in the summed throws profile (Vetterlein & Roberts, 2010). Here, G4 is ~435 km long and trends N100°E. It is divided into three main segments of 100–180 km long, separated by step overs >3 km wide. Each major segment of G4 is formed by 2–5 secondary segments of ~50 km long, mostly separated by 1–3 km
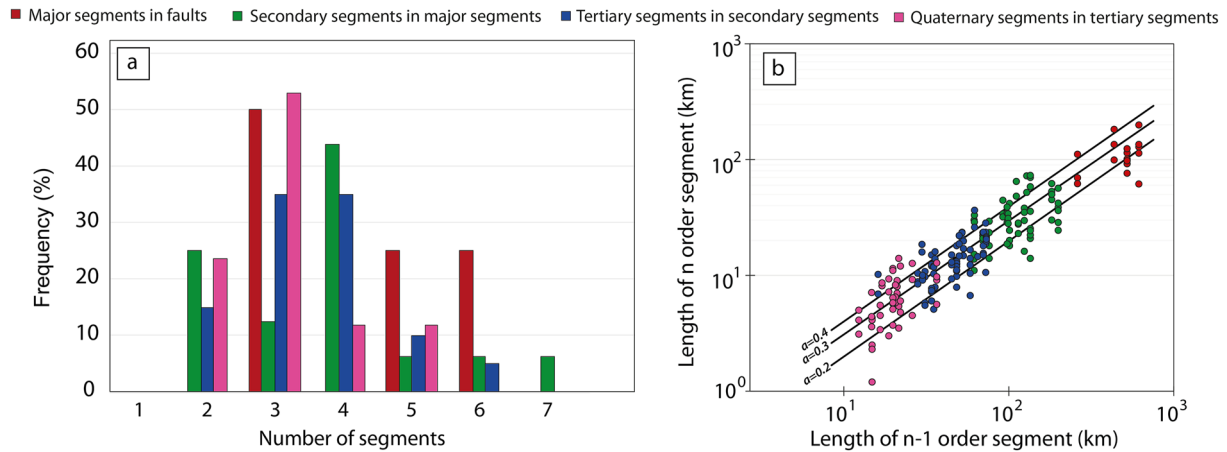
■ Major segments in faults   ■ Secondary segments in major segments   ■ Tertiary segments in secondary segments   ■ Quaternary segments in tertiary segments

Figure 4. (a) Frequency distribution of the number of segments/subsegments within faults/segments of the Cerberus Fossae fault system. (b) Relation between the length of each n-order segment as a function of the length of $(n - 1)$-order segment. The black lines are the linear relations $LS_n = a \times LS_{n-1}$ where a is a constant of proportionality ($a = 0.2$, 0.3, and 0.4).

step overs (inside major segments 2 and 3) or connected through slight bends of 20° in the surface trace (inside major segment 1). Inside most of the secondary segments (i.e., the isolated ones), it is possible to observe tertiary segments (Figure 3), which are ~15 km long on average and separated by slight changes in the azimuth (<10°) and smaller step overs (between 500 m and 1 km wide). Quaternary segments of ~7 km long on average are observed into several tertiary segments (Figure 3, Figure S1 in Supporting Information S1). They are separated by small step overs <300 m wide and azimuth changes <10°. Tertiary and quaternary segmentations are hardly distinguishable in the western parts of the G1 and G2 fossae, where major segments are well connected and thus the smaller scale discontinuities are smoothed out.

The complete analysis of the segmentation reveals that the different fossae in the Cerberus region are laterally segmented into a limited number of segments, that is, with a frequency between 2 and 7 segments/subsegments at every scale we observe, with a maximum of 3–4 segments/subsegments within fossae/segments (Figure 4a). We provide below some statistics about the number of segments we clearly identified (Figure 3, Figure S1 in Supporting Information S1). In many parts of the fossae, the evolved linkage along the surface trace makes it difficult to identify small segments (especially the tertiary and quaternary ones), preventing the potential identification of the total number of subsegments. We thus observe that 50% (2) of the fossae are divided into three major segments, 25% (1) into five major segments, and 25% (1) into six major segments. Since we consider only four fossae at this scale, these percentages have to be used with caution. More robust statistics can be obtained from the 16 major segments for those we identified secondary segments. It seems that ~25% (4) of the major segments are divided into two secondary segments, ~13% (2) into three secondary segments, ~44% (7) into four secondary segments, ~6% (1) into five secondary segments, ~6% (1) into six secondary segments, and ~6% (1) into seven secondary segments. The 60 secondary segments identified are themselves divided into two (15%), three (35%), four (35%), five (10%), and six tertiary segments (5%; for a total of 71 tertiary segments identified). Finally, 24% of the tertiary segments are divided into two quaternary segments, 53% into three quaternary segments, 12% into four quaternary segments, and 12% into five quaternary segments (for a total of 53 quaternary segments identified).

Figure 4b shows a complementary plot of the data, which represents the relation between the lengths of each scale of segmentation. The black linear relations $LS_n \sim (0.3 \pm 0.1) \times LS_{n-1}$ suggest that the fault/segments are subdivided into a similar number of segments/subsegments, which is about three (Figure 4b).

3.3. Lateral Morphological Variations of Cerberus Fossae

We use HiRISE stereo pair images to compute high-resolution DEMs along the Cerberus Fossae system (see locations on Figure 1b) using the SOCET SET mapping software (©BAE Systems). The stereo images are selected at different locations on the fossae in order to get an overall view of the lateral variation of the morphology along the Cerberus Fossae system. Stereo pairs were identified through ISIS image processing software package

(USGS). They are calibrated based on the HiRISE camera specifications, corrected from jitter effects by the USGS ISIS software and then implemented into SOCET SET. Bundle adjustment is made in an absolute reference frame defined by MOLA. The coarser first iteration of the DEM calculation is seeded on the gridded MOLA elevations at a resolution of 2 m/pixel. It is then followed by a refined DEM computation at higher resolution (up to 1 m/pixel). Postprocessing DEM corrections are performed on outlying points to discard aberrant calculations (see red and green areas on Figure 5 G1-A, G1-C, and G2-A). Figure 5 presents the resulting DEMs, for which we extract a series of topographic profiles across the fossae (Figure S2 in Supporting Information S1).

Fossae are fairly symmetrical with flat "rift shoulders," especially in the eastern and southern parts of the system along G3, G4, and G5. The latter fossae present a narrow fracture zone with steep slopes (~75–80°) and the minimum vertical throw and width of ~50 and ~100 m, respectively (see G4, Figure 5). The bottom of the fossae is mostly formed by a layer of sediments, but it is also possible to observe preserved flat ground surfaces that have subsided (G4B; Figure 5). On the other hand, the western fossae (G1 and G2) are wider (~1,000 m maximum) and deeper (~500 m maximum of depth), associated with several slope breaks in the topographic profiles (Figures 5 and 6, Figure S2 in Supporting Information S1). The lower parts are characterized by sediments eroded from the upper parts of the fossae and forming fan structures associated with shallow slopes (~30°; Figures 5 and 6, see also Vetterlein & Roberts, 2009). Steep slopes (~70°) situated above these fan structures form the main walls of the fossae (Figures 5 and 6, Figure S2 in Supporting Information S1). They are composed of more competent rocks (such as basalts, Jaeger et al., 2010; Plescia, 2003). At some locations, the steepest slopes are associated with erosional syntectonic morphologies, such as triangular facets (on G2; Roberts et al., 2012; Vetterlein & Roberts, 2009). We also observe similar morphologies along G1 (Figure 6), which are situated on the top of the steepest slopes we measure (G1-C; Figures 5 and 6a). They are different from common erosional spur and gully morphology (i.e., mass wasting without tectonic activity) that have been observed on the slopes of Martian troughs (e.g., Valles Marineris, Lucas et al., 2009; Nedell et al., 1987; Peulvast et al., 2001). While regular spurs and gullies show a sinuous base controlled in our case by subhorizontal lithological contrasts (Figure 6c), the base of the triangular facets follows a straight trend (Figures 6b and 6c), which we interpret as the surface expression of a possible highly dipping fault scarp (Burbank & Anderson, 2011). Similar morphologies have been observed in Valles Marineris on Mars (e.g., Peulvast et al., 2001). The Cerberus facets are about 200 m long and their base is 80 m wide, and they are characterized by layers of sediments, lava flows, and ashes from past volcanic activities (smoothed terrains in Figure 6; Tanaka et al., 1992). The area covered by the facets can extend over large distances away from the main fossa axis, where retrogressive erosion processes can be observed (G1-C, G2-A, and G3-B Figure 5; see also Pendleton, 2015). Altogether, these morphologies highlight the possible interactions between tectonic (i.e., graben formation) and erosional processes at the surface and subsurface (i.e., possible circulation of fluids induced by the melted cryosphere) that occurred in the evolution of Cerberus Fossae (see also discussion in Section 4).

In the upper parts of some fossae (G1 and G2), we observe a slight increase of the slope in the last few meters. This could mark the presence of materials harder than the underlying sediments, such as duricrust in the regolith close to the ground surface (Jakosky & Christensen, 1986).

We compile in Figures 7a and 7b the summed throw and mean width of the fossae, inferred from the mean topographic profiles from each HiRISE calculated DEM (see all mean profiles in Figure S2 in Supporting Information S1). It shows the difference in throw and width from west to east and north to south along Cerberus Fossae. G1 presents the largest throw and width (blue dots, Figure 7). The western part of G2 has similar width and throw than G1, but they decrease rapidly toward the east (see green dots). G3 follows a similar behavior, showing an overall smaller throw and width than G1 and G2, associated with a decrease of the relative throw and width toward the east (yellow dots, Figure 7). G4 (red dots) do not show clear lateral variation but they are, with G5 (brown dots), presenting the smallest widths and throws of the Cerberus Fossae system. Altogether, these observations show an overall decrease of the fossae dimension toward the east and the south. We also show in Figure 7c the MOLA elevations at each site. It is interesting to note that they decrease fairly linearly from west to east, contrasting with the large step seen in width and throw measurements between northwestern G1-G2 fossae and southeastern G3-G4-G5 fossae.

We estimate the summed throw values of fossa G1 from the three mean topographic profiles calculated for each DEM (Figure 5, Figure S2 in Supporting Information S1) and find a good agreement with the measurements done by Vetterlein and Roberts (2010) from MOLA data. In their study, they did not perform width measurements
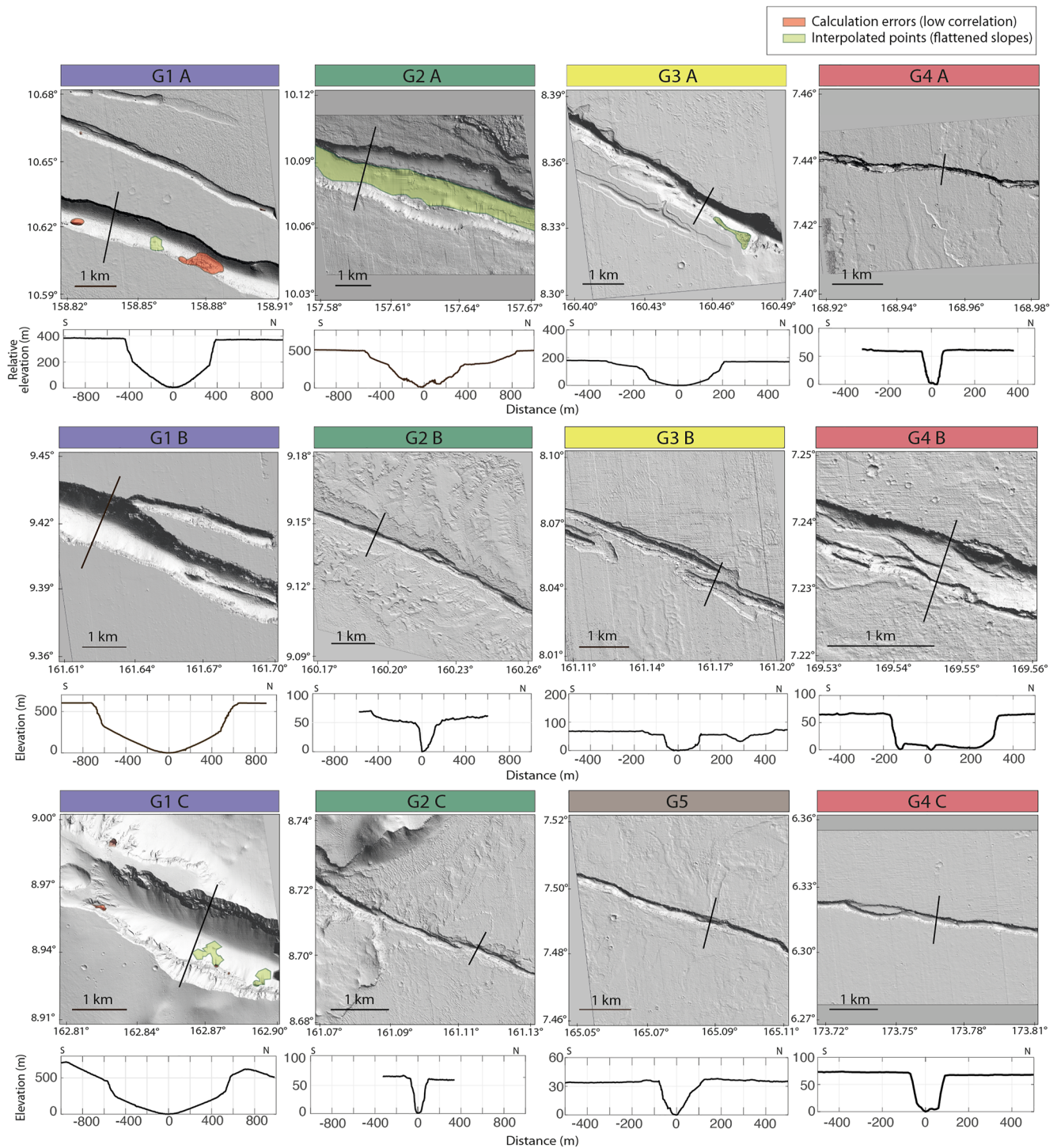
Figure 5. Digital Elevation Models (1 m/pixel) built from High-Resolution Imaging Science Experiment stereo pairs along the five main fossae (G1, G2, G3, G4, and G5) of Cerberus Fossae (see locations on Figure 1). One across strike relative topographic profile is shown below each DEM (see Figure S2 in Supporting Information S1 for all and mean profiles).

because the scarps are assumed to have undergone collapse (e.g., rockfalls and landslides) that widened them and which therefore could have affected their interpretation. Still, based on their throw measurements, we estimate a range of widths by measuring three different distances across the fossa: a "maximum" or "apparent" width (Wa; Figure 8), the width measured at the top of the triangular facets and/or expected fault scarp (i.e., the steepest
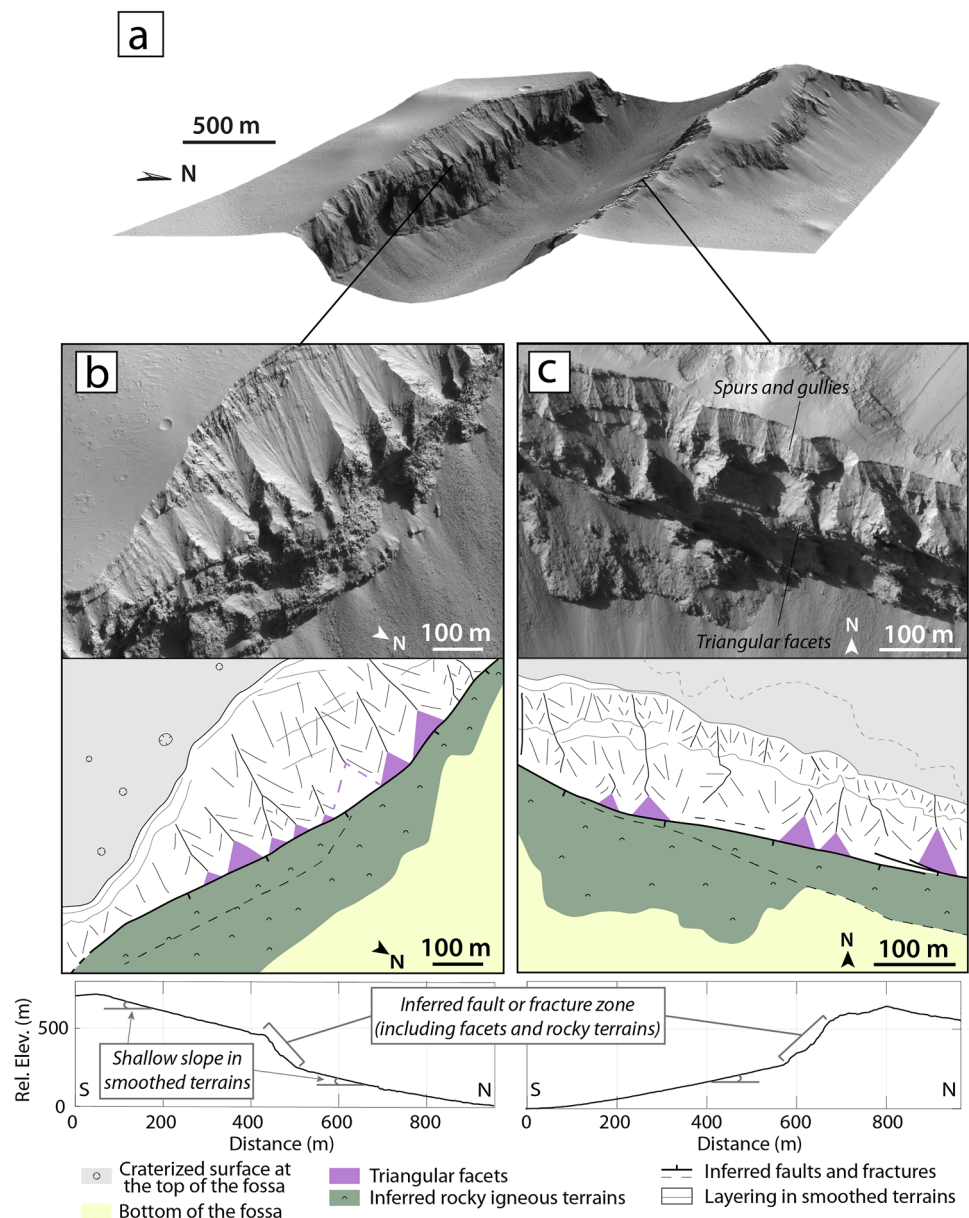
Figure 6. (a) 3D view built from stereo pair High-Resolution Imaging Science Experiment images (ESP_017719_1890; ESP_017218_1890) along G1 (see also G1A on Figure 5). Panels (b and c) are zooms along the edge of the fossa. Sketches highlight the triangular facets associated with the linear trends that we infer to be the main high-dipping fault traces, separating the green rocky materials (igneous and possibly brecciated rocks) from the white smoothed terrains (mix of ashes, igneous, and sedimentary rocks). Notice the difference between the morphology of the triangular facets and the spurs and gullies at the top of the fossae. Relative topographic profiles going through (b) and (c) show the slope breaks associated with the interpreted sketches (see the complete topographic profiles and corresponding imprints in map view in the middle of G1C in Figure S2 in Supporting Information S1).

slope; Wt; Figure 8), and the width measured at the base of the steepest slope (Wb; Figure 8). Thus, Wa encompasses the whole structure (including potential collapse and eroded material). In an ideal case with no erosion, Wt would be the best parameter representing the fossa width. Finally, Wb would represent a minimum structural width of the fossa. Wa and Wb give the range of fossa widths, which is a good proxy of the minimum and maximum uncertainties in our measurements. In order to have a full coverage of the fossa, we perform our analysis from CTX images at the locations of the measurements done by Vetterlein and Roberts (2010) from MOLA data tracks. The results are shown in Figure 9 and present the fossa width variations along G1. As expected, the largest
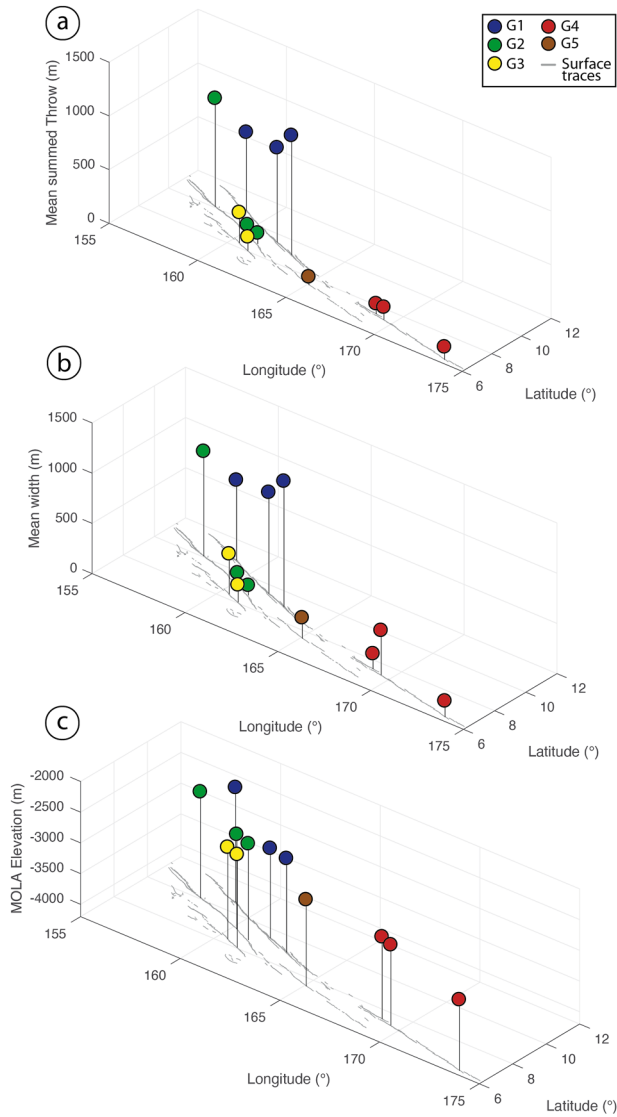
Figure 7. Mean (a) summed throw and (b) width of fossae deduced from each calculated DEM (see Figure 5, Figure S2 in Supporting Information S1), showing the general decrease from west and north (G1 and G2) to east and south (G3, G4, and G5). (c) Corresponding MOLA elevation. Gray lines are surface traces of Cerberus Fossae.
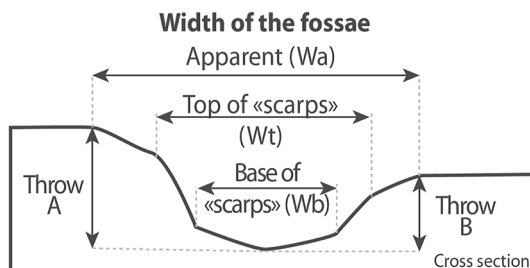

Figure 8. Schematic cross section of a fossa showing the different measurements performed in this study (see text for detail).

range of widths (i.e., between Wa and Wb; orange areas in Figure 9b) is observed along the sections accommodating the largest deformation, indicating a more evolved section of the fossa that has been submitted to erosional processes and collapse. On the other hand, along the most immature parts of the fossa (i.e., close to the tips), the range of widths is smaller, since the fossa shoulders are better preserved (Wa ~ Wt). The overall fossa width and summed throw profiles are equivalent (see Figures 9a and 9b). In Figure 9b, we did not measure the width associated with the subparallel segment situated between segments 5 and 6 (dotted lines in Figure 9a; segment labeled "9.1" in Vetterlein and Roberts (2010)) since it is not a colinear segment and seems to be an older fossa structure crosscut now by segment 5 (Figure S1 and Text S1 in Supporting Information S1). Figure 9c indicates that the fossa width (W) is two times the fossa throw ($W \sim 2 \times T$) if we consider that both throws are equal (northern and southern throws, Figure 8), which seem to be the case in most parts of the fossa. Note that some values show large width measurements for very small throws (gray area in Figure 9c). We consider these values as outliers since they are mostly situated near fault/segment tips where the small summed throw (<500 m) might be underestimated by non-resolved MOLA measurements.

4. Discussion

4.1. Evolution and Direction of Long-Term Propagation of Cerberus Fossae

We observe that Cerberus Fossae exhibit systematic changes in fossae widths and vertical throws from west to east (Figures 5 and 7). These observations are summarized in Figure 10: fossae are wider with higher vertical throw in the western and northern parts of the system (Figure 10b; G1 and G2) than in the eastern and southern parts (Figure 10b; G3, G4, and G5). This implies that the cumulative displacement accommodated by Cerberus Fossae decreases from the west(-northwest) to the east(-southeast) and suggests that deformation has propagated over the long term toward the east(-southeast) away from Elysium Mons situated to the northwest (Figure 1a). We suggest that the igneous activity beneath Elysium Mons was both the source for melts and regional tectonics stresses that were responsible for dike development and stress propagation toward the east(-southeast) at Cerberus Fossae. Other evidence supports this interpretation: the morphology also changes along strike. More mature fossae G1 and G2 seem to have been submitted to erosional processes (i.e., slope variation of the flank of the fossa, boulders, and triangular facets; see Figures 5 and 6) associated with sediment deposits (Figure 6; see also triangular facets in the western part of G2, Roberts et al. (2012) and Vetterlein and Roberts (2009)). Furthermore, assumed younger fossae G3, G4, and G5 are well preserved (homogeneous steep slopes of the flanks of the fossae; Figure 5), denoting a decreasing exposure time to surface processes from west to east. Additionally, fault segments are well connected in the western part of the fault system, while they are not in the eastern part (Figure 3, Figure S1 in Supporting Information S1). This indicates relatively longer activity of the dike-induced graben system in the west, where successive ruptures favored the linkage between dike at depth and fossa segments at the surface. Moreover, smaller scales of segmentation (i.e., tertiary and quaternary segmentation) are more observed in the eastern fossae (e.g., G4), representing the less evolved part of Cerberus Fossae (i.e., lesser degree of segment linkage in the eastern fossae).
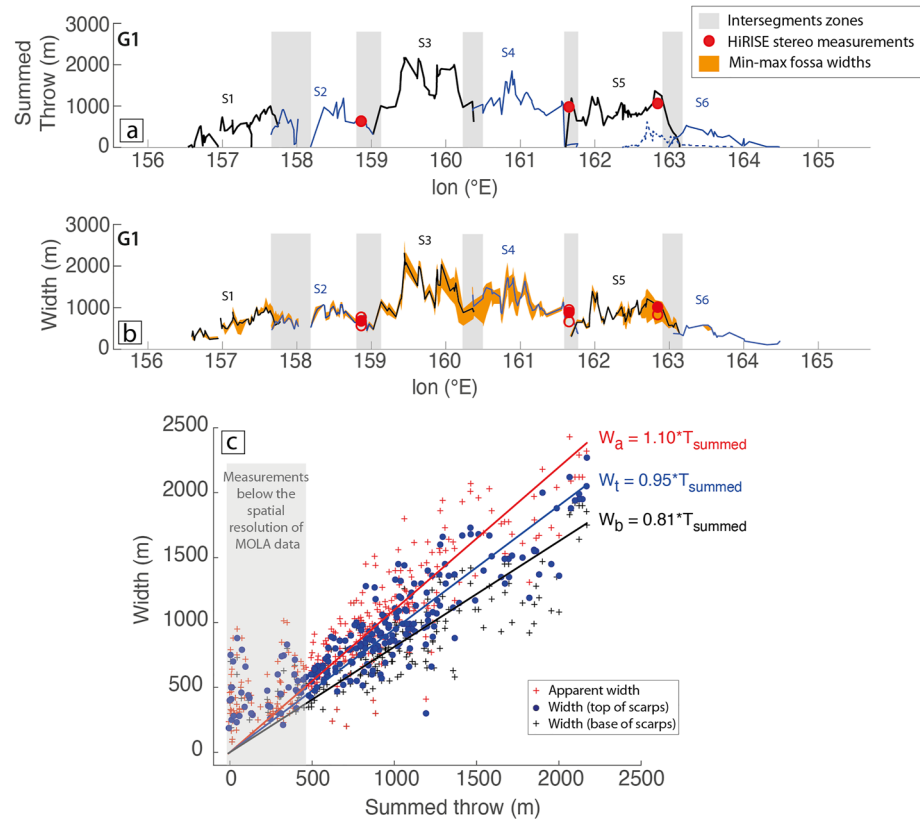
Figure 9. Along-strike measurements of throw and width for fossa G1. (a) Summed throw profile (MOLA data; Vetterlein and Roberts, 2010). (b) Corresponding fossa widths (this study, CTX data). Solid lines are preferred fossa widths (Wt; see text and Figure 8), while orange area is determined from maximum (Wa) and minimum (Wb) width measurements (see Figure 8). Solid red dots are preferred width measurements made on DEMs built from High-Resolution Imaging Science Experiment stereo pairs (Figure 5), while empty red dots are minimum and maximum width measurements. Alternate blue and black profiles represent the major segmentations identified in this study. They are separated by intersegment zones, highlighted by the gray rectangles (major slip trough, see also fault map in Figure S1 in Supporting Information S1); (c) Relations between the summed throw and the width of fossa G1. Blue dots are preferred fossa width values (Wt) and red and black crosses are maximum (Wa) and minimum (Wb) width values, respectively (see text and Figure 8). The three colored lines describe the linear law for each data set and suggest that the fossa Width ~ Summed Throw (linear correlation coefficient $R = 0.94$ for the preferred blue law, $R = 0.95$ for the red law, and $R = 0.92$ for the black law). Note that the gray-shaded area highlights the part of the plot where throw measurements are below the spatial resolution of MOLA data (i.e., 463 m/pixel). This explains why width measurements are possibly associated with possibly low underestimated throw measurements (see more details in the text).

The accumulation of stress and the eastern propagation of the dike system took place during a long period of time from the building of the slopes of Elysium Mons (peak of volcanic activity at 2.2 Gy; Platz & Michael, 2011) to the volcanic activity of the Central Elysium Plains at the origin of the fossae (from 250 to 2 My; Vaucher et al., 2009). However, stream lines and triangular facets are locally observed along the fossae, suggesting the action of fluids eroding their flanks. At some locations, triangular facets along G1 (Figure 6) seem to be situated on top of the steepest slopes, which could be comparable to hanging valleys on Earth (e.g., Burbank & Anderson, 2011). This morphology could be explained by three main (nonexclusive) mechanisms: (a) during the early formation of the fossae, the rise of the dikes interacting with shallow pressurized groundwater or cryosphere (e.g., Burr et al., 2002; Head et al., 2003; Pendleton, 2015; Plescia, 2003) and the resulting water floods eroded the early formed dike-induced fault scarps; (b) the opening rate of the fossae was significantly higher than the erosion rate; or (c) the slope breaks across the fossae highlight lithological contrasts between sediments (shallow slopes) and steep slopes (basalts), which would induce a differential erosion.

Our morphological observations (Figure 6) and the strong correlation between fossae width and throw (Figure 9) suggest that the fossae are structurally shallow graben bounded by steep walls. Note that the strike and inferred
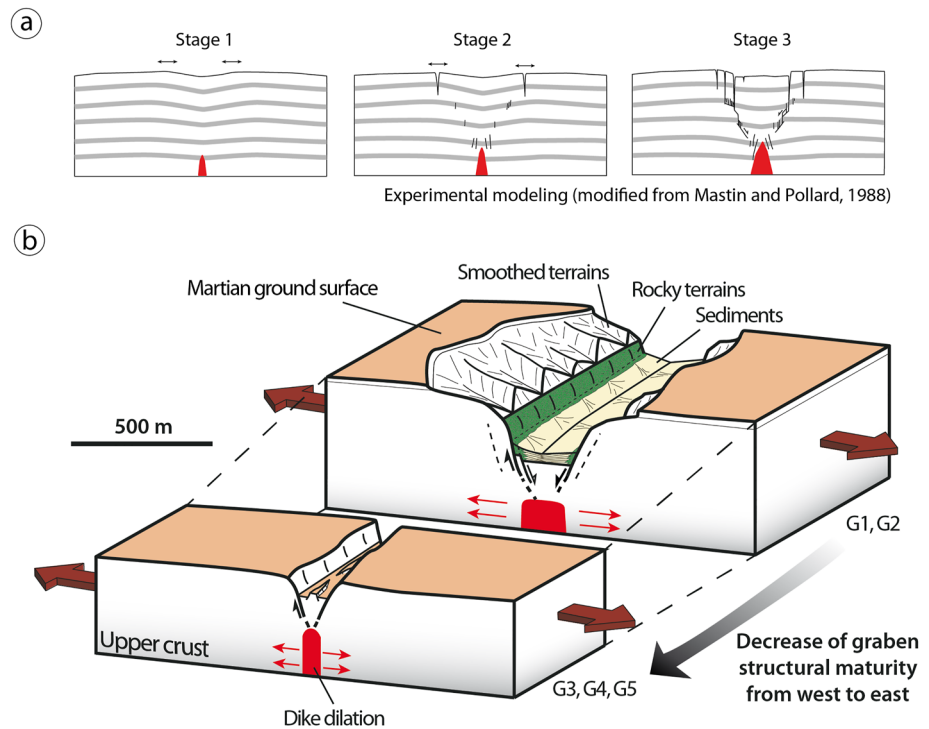
Figure 10. (a) Early stages of the evolution of fault and fracture growth above a shallow dike (modified from Mastin & Pollard, 1988). The progressive linkage of steep fractures (stages 1 and 2) leads to the formation of normal dip slip (stage 3). (b) Schematic representations and interpretations of the morphology and structure of Cerberus Fossae along its northwestern mature sections (G1 and G2) and southeastern immature sections (G3, G4, and G5).

dip are in good agreement with moment tensor solutions found by Brinkman et al. (2021) for recent marsquakes. It is unclear if these faults correspond to Mode II shearing cracks (i.e., steep normal faults) or are actually part of large Mode I opening cracks (joints) that would form the fossae. It is likely that both Modes are interacting each other in a complex pattern since the early formation of the graben as observed in experimental models (Figure 10a; e.g., Mastin & Pollard, 1988). The progressive linkage between first formed steep fissures at the surface and fractures at depth lead to the formation of normal dip slip responsible for the subsidence of the center part of the graben (stage 3; Figure 10a). The subsidence of the center parts of the Cerberus Fossae and the observation of the triangular facets support this shearing deformation. However, as said above, the rheological contrast between igneous rocks reaching the surface through the fractures and the surrounding material might also contribute to the formation of the facets.

Assuming that the actual fossae morphology is mainly due to dike propagation at depth, width measurements can be used to study the location and size of dikes at depth. The maximum fault heave is a proxy for dike thickness (e.g., Rubin & Pollard, 1988), which means that in our case, the fault heave would be half of the difference between Wt and Wb (i.e., the width at the top and the base of the steepest slope, respectively). Therefore, the dike thickness along G1 ranges from 8 to 375 m with an average width of ~49 m. The maximum dike thickness is situated where the fossae width and throw are maximum close to the center part of G1 (Figure 9). Those values might be underestimated since the top and the bottom of the fault scarp are eroded and/or covered under sediments layer, respectively (Figure 10b).

Also, graben half width is a proxy of dike upper tip depth (Hjartardóttir et al., 2016; Magee & Jackson, 2021; Pollard et al., 1983; Trippanera et al., 2015), which in our case would imply an average depth of ~488 m in the center part of G1, decreasing slightly toward the west (~300 m) and strongly toward the east (~90 m). These depths might highlight heterogeneities and shallow layering in the subsurface that would affect the dike emplacement at depth (see also the following section). Note also that the regional elevation decreases fairly linearly from west to east (Figures 1b and 7c), which might imply that dike upper tips could be located at a constant depth (or elevation) that would affect the fossa widths at surface. However, the decrease in width and throw is not linear

and shows a major step between G1, G2 and G3, G4, and G5 (Figures 7a and 7b), suggesting possible variations in dike locations at depth. In any case, if this relation is correct, the small fossa widths (eastern tips of fossae G1, G2 and fossae G3, G4, and G5) would indicate the location where the dikes are close to the surface.

4.2. Generic Segmentation Along Cerberus Fossae

4.2.1. Comparison With Terrestrial Faults and Implications for Fault Growth

Detailed analysis of the Cerberus Fossae system shows that the along-strike segmentation is not random, but is similar at its four largest scales (i.e., 3–4 segments at each scale; Figure 4). These results are equivalent to the number of major segments and secondary segments found for a large population of normal faults in Afar (rifting context on Earth) but also along-reverse and strike-slip faults (Manighetti et al., 2015 and references therein). These similar observations support the idea that Cerberus Fossae are faults and fractures and that their growth process on Mars is similar than on Earth. Graben segmentation at the surface is intimately linked to dike emplacement at depth (Pollard et al., 1983) and more particularly dike thickness changes occurring at depth during phases of dike propagation (e.g., Magee & Jackson, 2021 and references therein). In our case, the eastward propagation of dikes from Elysium Mons probably occurred by the successive formation of new dike segments at the eastern tip of the existing ones (Healy et al., 2018; Rubin, 1995; Townsend et al., 2017). The new dike segment lengthens rapidly and widens until reaching a critical thickness that could trigger surface faulting and fracturing at its top (Trippanera et al., 2015). We infer minimum dike thickness as low as 8 m on G1; thus, it is necessary that the top of the dike reaches shallow depths to induce surface faulting (∼90 m estimated at the eastern tip). This propagation process is similar to normal fault growth on Earth, where phases of displacement accumulation occurring at constant length (Bull et al., 2006; Giba et al., 2012; Nicol et al., 2005) alternate with phases of lateral fault propagation through the formation of new fault segments (e.g., Manighetti et al., 2015 and references therein). The absence of plate tectonics and the presence of a thick, rigid lithosphere on Mars would favor the propagation of the dike over long distances and would promote fracture linkage at surface near Elysium Mons (i.e., thicker dikes and more evolved fossae), while isolated offset segments are located near the eastern propagating tips (i.e., thinner dikes and less evolved fossae).

Our definition of segments along G1 is slightly different from that defined by Vetterlein and Roberts (2010). In their study, they measured vertical throw from MOLA data and identified nine to 10 colinear segments, regardless of their length, separated by cumulative slip troughs in the summed throw profile (Figure 9a). Thus, they obtain more small isolated segments near the fossa tips, while longer ones are situated in the central parts of the fossa. However, their throw profile (Figure 9a) shows that inside each segment, secondary peaks and troughs are observed, indicating subsegments contained in the major segments (e.g., Manighetti et al., 2015). Since they are separated by smaller step overs and slip troughs compared to the other major segments we identified, we consider that the four western segments determined by Vetterlein and Roberts (2010) are secondary segments of major segment 1 (Figure 9, Figure S1 in Supporting Information S1). The other center and eastern major segments we defined are in fairly good agreement with their study. Nevertheless, future work is needed to better characterize the throw and width variations along all fossae (i.e., complete CTX DEM of the Cerberus Fossae fault system), since high-resolution data are mandatory to fully describe fault segmentation and propagation (Ze & Alves, 2019).

Segment length is often related to the depth of underlying heterogeneities, such as rheological and mechanical contrasts. For instance, previous studies on Earth described a relation between the length of fault segments (deduced from rupture traces of large continental earthquakes) and the thickness of the brittle seismogenic layer (∼18 ± 5 km on Earth; Klinger, 2010). Using experimental and numerical models, Lefevre et al. (2020) and Jiao et al. (2021) have also, respectively, shown that the inter-Riedel distance (or assumed segment length) is dependent on the brittle material thickness. On Mars, thermal models of the Martian interior estimated before the InSight landing a seismogenic lithospheric thickness from 30 to 100 km (Plesa et al., 2018) to 40–150 km (Knapmeyer et al., 2006). After the InSight landing, Knapmeyer-Endrun et al. (2021) have shown that the crustal thickness below the lander would range between 24 and 39 km (extrapolated from gravimetric data from 24 to 72 km for the whole planet), including a major discontinuity at 6–11 km deep (transition from highly altered and fractured to unfractured rocks). Along the Cerberus Fossae system, four scales of segmentation are identified in this study with an average length of ∼7 km for the quaternary segments (Figure 4b). Based on the studies cited above, it is unlikely that this value is related to the thickness of the seismogenic crust. However, it could be related

to the shallower layer identified by Knapmeyer-Endrun et al. (2021) at the InSight landing site, indicating that the changes in the rock lithologies/properties with depth could extend to further regions on Mars. The mean length of major, secondary, and tertiary segments is 112, 36, and 15 km, respectively. While the mean length of secondary segments is included in the range of Moho depth inferred on Mars (Knapmeyer-Endrun et al., 2021), the length of major and tertiary segments could highlight other possible discontinuities at depth.

4.2.2. Regional and Local Stress Concentrations: Constraints on Marsquake Locations Recorded by the InSight Mission

The first results of the InSight mission have shown that locating marsquake epicenters using one seismic station is very challenging. While most of the major quakes seem to come from the Cerberus region (e.g., Clinton et al., 2021; Giardini et al., 2020), the location uncertainties remain significant (about $\pm 3°$ and $\pm 10°$ in epicentral distances and azimuth, respectively). Our study provides some strong constraints that could be used to better define the location of tectonic marsquakes. Indeed, it is well known that fault and fracture segmentation has an impact on stress distribution (e.g., Barka & Kadinsky-Cade, 1988; Crider & Pollard, 1998; de Joussineau & Aydin, 2009; Manighetti et al., 2009, 2015; Saucier et al., 1992; Segall & Pollard, 1980; Soliva & Benedicto, 2004). While aftershocks occur usually at the edges of high coseismic slip patches or in regions of low coseismic slip (e.g., Mendoza & Hartzell, 1988), a significant amount of small seismic events take place in the intersegment zones (e.g., Liu et al., 2003). They correspond to areas of long-term slip deficit where heterogeneous types of faults and fractures are present and residual stresses concentrate. Thus, they are likely to trigger potential seismic events, which are useful in the context of the InSight mission. Most of the faults on Mars were formed during its main active period, more than 3 Gy ago (Anderson et al., 2008; Carr & Head, 2010; Schubert et al., 1990). Currently, those faults are not likely to experience high strain rates due to the lack of plate tectonics. Until InSight, recent strains on Mars were expected to be dominated by thermal contraction of the planet (Taylor et al., 2013). The recent joint discoveries of seismic events with extensional slip motion localized at Cerberus (Brinkman et al., 2021), detection of low-frequency events possibly associated with lava circulation at depth (Kedar et al., 2021), and geological evidences of recent (<1 Ma) volcanic activity (Horvath et al., 2021) suggest active ongoing volcano-tectonic activity along Cerberus Fossae. On Earth, a simple model of a circular rupture is assumed for small shallow earthquakes (i.e., $M_w < 7.5$), leading to scaling relations between the rupture length and the seismic moment, such as $M_0 \propto L^3$ (Aki & Richards, 2002; Denolle & Shearer, 2016; Scholz, 2019). It results in an average rupture length of 1 km for an M_w 3.5 earthquake similar to the magnitudes of the largest events observed by InSight. Therefore, if this law is valid in the Martian context, the larger events detected so far by InSight would not be able to break entirely the smallest segments (i.e., quaternary) identified in this study (Figure 4b). This gives insights on the spatial scale to look for surface deformations triggered by the marsquakes (rockfalls and landslide) from new orbital data. Roberts et al. (2012) estimated rupture length of paleomarsquakes from fallen boulder populations along Cerberus Fossae (fossa G2). It seems unlikely that the ~100 km surface ruptures they defined have been formed by a single large event, but rather by a series of smaller events that generated a maximum rupture length at kilometric scales. The potential recent activity highlighted by Roberts et al. (2012) in a restricted area might reflect cluster of moderate-size events occurring in a short time period as compared to their mean recurrence interval (e.g., Scholz, 2019).

Assuming an active context of dike and fracture propagation along Cerberus Fossae, we can expect that most of the seismicity will be located at shallow depth, since on Earth it occurs mostly between the upper dike top and the surface (Ágústsdóttir et al., 2016; Passarelli et al., 2015; Rubin & Gillard, 1998; Ukawa & Tsukahara, 1996). However, the estimated first results from the InSight mission suggest hypocentral depths of 20–30 km for the main events (e.g., Brinkman et al., 2021; Stähler et al., 2021). On the other hand, the lateral propagation of the system toward the east implies that the seismicity could be also located at depth near the propagating dike tips (Green et al., 2015; Rubin & Gillard, 1998; Sigmundsson et al., 2015). Indeed, Rivas-Dorado et al. (2021) have shown that Martian conditions are favorable to develop giant dike systems (e.g., Elysium Fossae) that could reach much greater depths (15–20 km).

5. Conclusions

We performed a detailed mapping and structural analysis of the Cerberus Fossae system based on HiRISE and CTX images, in addition to stereo pair images used to calculate high-resolution DEMs. The relation between fossa width and throw supports volcano-tectonic processes as the main origin of fossae formation. They would have

formed by the propagation of dikes at depth, possibly related to the rise of Elysium Mons, located further to the NW. The analysis of the lateral segmentation at the surface highlights up to four scales of segments. Most of the fossae/segments are divided into three to four segments/subsegments as it has been observed on Earth. The overall linkage between segments decreases from west to east as do the overall fossae widths and throws. Altogether, these evidences are in good agreement with a long-term direction of dike-induced fault propagation toward the east. In the frame of the InSight mission, our study helps to identify the zones of potential seismic activity at the regional scale (i.e., expected increase of seismicity toward the east where the fossae are immature) and the local scale (i.e., in intersegment zones where stress concentrations likely occur).

Data Availability Statement

The data used in this study are available at the NASA PDS Imaging Node, Mars Reconnaissance Orbiter Online Data Volumes (https://pds-geosciences.wustl.edu/missions/mro/; Malin (2007) and McEwen (2007) for CTX and HiRISE images, respectively). The calculated DEMs and measurements (segmentation, width, and throw) are available on Zenodo (https://doi.org/10.5281/ZENODO.5618250; Perrin et al., 2021).

References

Ágústsdóttir, T., Woods, J., Greenfield, T., Green, R. G., White, R. S., Winder, T., et al. (2016). Strike-slip faulting during the 2014 Bárðarbunga-Holuhraun dike intrusion, central Iceland. *Geophysical Research Letters*, *43*(4), 1495–1503. https://doi.org/10.1002/2015GL067423

Aki, K. (1979). Characterization of barriers on an earthquake fault. *Journal of Geophysical Research*, *84*(B11), 6140–6148. https://doi.org/10.1029/jb084ib11p06140

Aki, K., & Richards, P. (2002). *Quantitative seismology*. University Science Books.

Anderson, R. C., Dohm, J. M., Haldemann, A. F. C., Pounders, E., Golombek, M. P., & Castano, A. (2008). Centers of tectonic activity in the eastern hemisphere of Mars. *Icarus*, *195*(2), 537–546. https://doi.org/10.1016/j.icarus.2007.12.027

Banerdt, W. B., Smrekar, S. E., Banfield, D., Giardini, D., Golombek, M., Johnson, C. L., et al. (2020). Initial results from the InSight mission on Mars. *Nature Geoscience*, *13*(3), 183–189. https://doi.org/10.1038/s41561-020-0544-y

Barka, A., & Kadinsky-Cade, K. (1988). Strike-slip fault geometry in Turkey. *Tectonics*, *7*(3), 663–684. https://doi.org/10.1029/TC007i003p00663

Berman, D. C., & Hartmann, W. K. (2002). Recent fluvial, volcanic, and tectonic activity on the Cerberus Plains of Mars. *Icarus*, *159*(1), 1–17. https://doi.org/10.1006/icar.2002.6920

Biasi, G. P., & Wesnousky, S. G. (2016). Steps and gaps in ground ruptures: Empirical bounds on rupture propagation. *Bulletin of the Seismological Society of America*, *106*(3), 1110–1124. https://doi.org/10.1785/0120150175

Biasi, G. P., & Wesnousky, S. G. (2017). Bends and ends of surface ruptures. *Bulletin of the Seismological Society of America*, 1–18. https://doi.org/10.1785/0120160292

Böse, M., Clinton, J. F., Ceylan, S., Euchner, F., van Driel, M., Khan, A., et al. (2017). A probabilistic framework for single-station location of seismicity on Earth and Mars. *Physics of the Earth and Planetary Interiors*, *262*, 48–65. https://doi.org/10.1016/j.pepi.2016.11.003

Brinkman, N., Stähler, S. C., Giardini, D., Schmelzbach, C., Khan, A., Jacob, A., et al. (2021). First focal mechanisms of marsquakes. *Journal of Geophysical Research: Planets*, *126*(4). https://doi.org/10.1029/2020JE006546

Bull, J. M., Barnes, P. M., Lamarche, G., Sanderson, D. J., Cowie, P. A., Taylor, S. K., & Dix, J. K. (2006). High-resolution record of displacement accumulation on an active normal fault: Implications for models of slip accumulation during repeated earthquakes. *Journal of Structural Geology*, *28*(7), 1146–1166. https://doi.org/10.1016/j.jsg.2006.03.006

Burbank, D. W., & Anderson, R. C. (2011). *Tectonic geomorphology*. John Wiley & Sons.

Burr, D. M., Grier, J. A., McEwen, A. S., & Keszthelyi, L. P. (2002). Repeated aqueous flooding from the Cerberus Fossae: Evidence for very recently extant, deep groundwater on Mars. *Icarus*, *159*(1), 53–73. https://doi.org/10.1006/icar.2002.6921

Carr, M. H., & Head, J. W. (2010). Geologic history of Mars. *Earth and Planetary Science Letters*, *294*(3–4), 185–203. https://doi.org/10.1016/j.epsl.2009.06.042

Cassanelli, J. P., & Head, J. W. (2018). Large-scale lava-ice interactions on Mars: Investigating its role during late Amazonian central Elysium Planitia volcanism and the formation of Athabasca Valles. *Planetary and Space Science*, *158*(April), 96–109. https://doi.org/10.1016/j.pss.2018.04.024

Ceylan, S., Clinton, J. F., Giardini, D., Böse, M., Charalambous, C., van Driel, M., et al. (2021). Companion guide to the marsquake catalog from InSight, Sols 0–478: Data content and non-seismic events. *Physics of the Earth and Planetary Interiors*, *310*, 106597. https://doi.org/10.1016/j.pepi.2020.106597

Clinton, J. F., Ceylan, S., van Driel, M., Giardini, D., Stähler, S. C., Böse, M., et al. (2021). The marsquake catalogue from InSight, Sols 0–478. *Physics of the Earth and Planetary Interiors*, *310*(October 2020), 106595. https://doi.org/10.1016/j.pepi.2020.106595

Clinton, J. F., Giardini, D., Böse, M., Ceylan, S., van Driel, M., Euchner, F., et al. (2018). The marsquake service: Securing daily analysis of SEIS data and building the Martian seismicity catalogue for InSight. *Space Science Reviews*, *214*(8), 133. https://doi.org/10.1007/s11214-018-0567-5

Crider, J. G., & Pollard, D. D. (1998). Fault linkage: Three-dimensional mechanical interaction between echelon normal faults. *Journal of Geophysical Research*, *103*(B10), 24373–24391. https://doi.org/10.1029/98JB01353

Daubar, I., Lognonné, P., Teanby, N. A., Miljkovic, K., Stevanović, J., Vaubaillon, J., et al. (2018). Impact-seismic investigations of the InSight mission. *Space Science Reviews*, *214*(8), 132. https://doi.org/10.1007/s11214-018-0562-x

de Joussineau, G., & Aydin, A. (2009). Segmentation along strike-slip faults revisited. *Pure and Applied Geophysics*, *166*(10–11), 1575–1594. https://doi.org/10.1007/s00024-009-0511-4

Denolle, M. A., & Shearer, P. M. (2016). New perspectives on self-similarity for shallow thrust earthquakes. *Journal of Geophysical Research: Solid Earth*, *121*(9), 6533–6565. https://doi.org/10.1002/2016JB013105

Donzé, F. V., Klinger, Y., Bonilla-Sierra, V., Duriez, J., Jiao, L., & Scholtès, L. (2021). Assessing the brittle crust thickness from strike-slip fault segments on Earth, Mars and Icy moons. *Tectonophysics*, *805*(February). https://doi.org/10.1016/j.tecto.2021.228779

Ernst, R., Grosfils, E., & Mège, D. (2002). Giant Dike Swarms: Earth, Venus, and Mars. *Annual Review of Earth and Planetary Sciences*, *29*(1), 489–534. https://doi.org/10.1146/annurev.earth.29.1.489

Giardini, D., Lognonné, P., Banerdt, W. B., Pike, W. T., Christensen, U., Ceylan, S., et al. (2020). The seismicity of Mars. *Nature Geoscience*, *13*(3), 205–212. https://doi.org/10.1038/s41561-020-0539-8

Giba, M., Walsh, J. J., & Nicol, A. (2012). Segmentation and growth of an obliquely reactivated normal fault. *Journal of Structural Geology*, *39*, 253–267. https://doi.org/10.1016/j.jsg.2012.01.004

Golombek, M., Warner, N. H., Grant, J. A., Hauber, E., Ansan, V., Weitz, C. M., et al. (2020). Geology of the InSight landing site on Mars. *Nature Communications*, *11*(1), 1014. https://doi.org/10.1038/s41467-020-14679-1

Green, R. G., Greenfield, T., & White, R. S. (2015). Triggered earthquakes suppressed by an evolving stress shadow from a propagating dyke. *Nature Geoscience*, *8*(8), 629–632. https://doi.org/10.1038/ngeo2491

Grindrod, P. M., Hollingsworth, J., Ayoub, F., & Hunt, S. A. (2018). The search for active marsquakes using subpixel coregistration and correlation: Best practice and first results. *Journal of Geophysical Research: Planets*, *123*(7), 1881–1900. https://doi.org/10.1029/2018JE005649

Gudmundsson, A. (1984). Tectonic aspects of dykes in Northwestern Iceland. *Jökull Journal*, *34*, 81–96.

Hall, J. L., Solomon, S. C., & Head, J. W. (1986). Elysium region, Mars: Tests of lithospheric loading models for the formation of tectonic features. *Journal of Geophysical Research*, *91*(B11), 11377. https://doi.org/10.1029/jb091ib11p11377

Hauber, E., Jonas, T., Voelker, M., Knapmeyer, M., Grott, M., & Matz, K.-D. (2014). Fault scaling on Mars: Slip distribution and displacement-length relationship derived from HRSC data. *45th Lunar and Planetary Science Conference*. https://doi.org/10.1002/jgre.20118

Head, J. W., Wilson, L., & Mitchell, K. L. (2003). Generation of recent massive water floods at Cerberus Fossae, Mars by dike emplacement, cryospheric cracking, and confined aquifer groundwater release. *Geophysical Research Letters*, *30*(11), 2–5. https://doi.org/10.1029/2003GL017135

Healy, D., Rizzo, R., Duffy, M., Farrell, N., Hole, M., & Muirhead, D. (2018). Field evidence for the lateral emplacement of igneous dykes: Implications for 3D mechanical models and the plumbing beneath fissure eruptions. *Volcanica*, *1*(2), 85–105. https://doi.org/10.30909/vol.01.02.85105

Hjartardóttir, Á. R., Einarsson, P., Gudmundsson, M. T., & Högnadóttir, T. (2016). Fracture movements and graben subsidence during the 2014 Bárðarbunga dike intrusion in Iceland. *Journal of Volcanology and Geothermal Research*, *310*, 242–252. https://doi.org/10.1016/j.jvolgeores.2015.12.002

Horvath, D. G., Moitra, P., Hamilton, C. W., Craddock, R. A., & Andrews-Hanna, J. C. (2021). Evidence for geologically recent explosive volcanism in Elysium Planitia, Mars. *Icarus*, *365*(February), 114499. https://doi.org/10.1016/j.icarus.2021.114499

Jaeger, W. L., Keszthelyi, L. P., Skinner, J. A., Milazzo, M. P., McEwen, A. S., Titus, T. N., et al. (2010). Emplacement of the youngest flood lava on Mars: A short, turbulent story. *Icarus*, *205*(1), 230–243. https://doi.org/10.1016/j.icarus.2009.09.011

Jakosky, B. M., & Christensen, P. R. (1986). Global duricrust on Mars: Analysis of remote-sensing data. *Journal of Geophysical Research*, *91*(B3), 3547–3559. https://doi.org/10.1029/JB091iB03p03547

Jiao, L., Klinger, Y., & Scholtès, L. (2021). Fault segmentation pattern controlled by thickness of brittle crust. *Geophysical Research Letters*, *48*(19), 1–7. https://doi.org/10.1029/2021gl093390

Kedar, S., Panning, M. P., Smrekar, S. E., Stähler, S. C., King, S. D., Golombek, M. P., et al. (2021). Analyzing low frequency seismic events at Cerberus Fossae as long period volcanic quakes. *Journal of Geophysical Research: Planets*, *126*(4), 1–28. https://doi.org/10.1029/2020JE006518

Klinger, Y. (2010). Relation between continental strike-slip earthquake segmentation and thickness of the crust. *Journal of Geophysical Research*, *115*(B7), B07306. https://doi.org/10.1029/2009JB006550

Knapmeyer, M., Oberst, J., Hauber, E., Wählisch, M., Deuchler, C., & Wagner, R. (2006). Working models for spatial distribution and level of Mars' seismicity. *Journal of Geophysical Research*, *111*(11), 1–23. https://doi.org/10.1029/2006JE002708

Knapmeyer-Endrun, B., Panning, M. P., Bissig, F., Joshi, R., Khan, A., Kim, D., et al. (2021). Thickness and structure of the Martian crust from InSight seismic data. *Science*, *373*(6553), 438–443. https://doi.org/10.1126/science.abf8966

Lefevre, M., Souloumiac, P., Cubas, N., & Klinger, Y. (2020). Experimental evidence for crustal control over seismic fault segmentation. *Geology*, *48*(8), 844–848. https://doi.org/10.1130/G47115.1

Leprince, S., Barbot, S., Ayoub, F., & Avouac, J. P. (2007). Automatic and precise ortho-rectification, coregistration, and subpixel correlation of satellite images, application to ground deformation measurements. *IEEE Transactions on Geoscience and Remote Sensing*, *45*(6), 1529–1558. https://doi.org/10.1109/tgrs.2006.888937

Liu, J., Sieh, K., & Hauksson, E. (2003). A structural interpretation of the aftershock "Cloud" of the 1992 Mw 7.3 landers earthquake. *Bulletin of the Seismological Society of America*, *93*(3), 1333–1345. https://doi.org/10.1785/0120020060

Lognonné, P., Banerdt, W. B., Giardini, D., Pike, W. T., Christensen, U., Laudet, P., et al. (2019). SEIS: Insight's seismic experiment for internal structure of Mars. *Space Science Reviews*, *215*(1), 12. https://doi.org/10.1007/s11214-018-0574-6

Lognonné, P., Banerdt, W. B., Pike, W. T., Giardini, D., Christensen, U., Garcia, R. F., et al. (2020). Constraints on the shallow elastic and anelastic structure of Mars from InSight seismic data. *Nature Geoscience*, *13*(3), 213–220. https://doi.org/10.1038/s41561-020-0536-y

Lucas, A., Ansan, V., & Mangold, N. (2009). New insight on genetic links between outflows and chasmata on Valles Marineris plateau, Mars. *Géomorphologie: Relief, Processus, Environnement*, *15*(1), 33–46. https://doi.org/10.4000/geomorphologie.7485

Magee, C., & Jackson, C. A. L. (2021). Can we relate the surface expression of dike-induced normal faults to subsurface dike geometry? *Geology*, *49*(4), 366–371. https://doi.org/10.1130/G48171.1

Malin, M. C. (2007). *MRO context camera experiment data record level 0 V1.0* (MRO-M-CTX-2-EDR-L0-V1.0). NASA Planetary Data System. https://doi.org/10.17189/1520266

Malin, M. C., Bell, J. F., Cantor, B. A., Caplinger, M. A., Calvin, W. M., Clancy, R. T., et al. (2007). Context camera investigation on board the Mars reconnaissance orbiter. *Journal of Geophysical Research*, *112*(E5), E05S04. https://doi.org/10.1029/2006JE002808

Manighetti, I., Campillo, M., Bouley, S., & Cotton, F. (2007). Earthquake scaling, fault segmentation, and structural maturity. *Earth and Planetary Science Letters*, *253*(3–4), 429–438. https://doi.org/10.1016/j.epsl.2006.11.004

Manighetti, I., Caulet, C., De Barros, D., Perrin, C., Cappa, F., & Gaudemer, Y. (2015). Generic along-strike segmentation of Afar normal faults, East Africa: Implications on fault growth and stress heterogeneity on seismogenic fault planes. *Geochemistry, Geophysics, Geosystems*, *16*, 443–467. https://doi.org/10.1002/2014GC005691.Received

Manighetti, I., Zigone, D., Campillo, M., & Cotton, F. (2009). Self-similarity of the largest-scale segmentation of the faults: Implications for earthquake behavior. *Earth and Planetary Science Letters*, *288*(3–4), 370–381. https://doi.org/10.1016/j.epsl.2009.09.040

Mastin, L. G., & Pollard, D. D. (1988). Surface deformation and shallow dike intrusion processes at Inyo Craters, Long Valley, California. *Journal of Geophysical Research*, *93*(B11). https://doi.org/10.1029/jb093ib11p13221

McEwen, A. S. (2007). *Mars reconnaissance orbiter high resolution imaging science experiment* (Reduced data record, MRO-M-HIRISE-3-RDR-V1.0). NASA Planetary Data System. Retrieved from https://pds-geosciences.wustl.edu/missions/mro/

McEwen, A. S., Eliason, E. M., Bergstrom, J. W., Bridges, N. T., Hansen, C. J., Delamere, W. A., et al. (2007). Mars reconnaissance orbiter's high resolution imaging science experiment (HiRISE). *Journal of Geophysical Research*, *112*(5), 1–40. https://doi.org/10.1029/2005JE002605

Mendoza, C., & Hartzell, S. H. (1988). Aftershock patterns and main shock faulting. *Bulletin of the Seismological Society of America*, *78*(4), 1438–1449. https://doi.org/10.1785/bssa0780031092

Nahm, A. L., Kattenhorn, S. A., & Pendleton, M. W. (2015). Unraveling the formation mechanism(s) of the Cerberus Fossae, Mars: Evacuated dikes, graben, or both? *Lunar and Planetary Science Conference*, *46*, 2367.

Nahm, A. L., Pendleton, M. W., & Kattenhorn, S. A. (2016). Cerberus Fossae, Mars: The case for dike intrusion-related formation and modification. *Acta Geologica Sinica – English Edition*, *90*(s1), 173–174. https://doi.org/10.1111/1755-6724.12957

Nedell, S. S., Squyres, S. W., & Andersen, D. W. (1987). Origin and evolution of the layered deposits in the Valles Marineris, Mars. *Icarus*, *70*, 409–441. https://doi.org/10.1016/0019-1035(87)90086-8

Nicol, A., Walsh, J. J., Berryman, K., & Nodder, S. (2005). Growth of a normal fault by the accumulation of slip over millions of years. *Journal of Structural Geology*, *27*(2), 327–342. https://doi.org/10.1016/j.jsg.2004.09.002

Panning, M. P., Lognonné, P., Bruce Banerdt, W., Garcia, R., Golombek, M. P., Kedar, S., et al. (2017). Planned products of the Mars structure service for the InSight mission to Mars. *Space Science Reviews*, *211*(1–4), 611–650. https://doi.org/10.1007/s11214-016-0317-5

Passarelli, L., Rivalta, E., Cesca, S., & Aoki, Y. (2015). Stress changes, focal mechanisms, and earthquake scaling laws for the 2000 dike at Miyakejima (Japan). *Journal of Geophysical Research: Solid Earth*, *120*(6), 4130–4145. https://doi.org/10.1002/2014JB011504

Pendleton, M. W. (2015). *Geomorphic evidence for geologically recent groundwater flow associated with the Cerberus Fossae magmatic and volcanic system, Mars*. University of Idaho.

Perrin, C., Jacob, A., Lucas, A., Myhill, R., Hauber, E., Batov, A., et al. (2021). Geometry and segmentation of Cerberus Fossae, Mars: Implications for marsquake properties. https://doi.org/10.5281/ZENODO.5618250

Peulvast, J.-P., Mège, D., Chiciak, J., Costard, F., & Masson, P. L. (2001). Morphology, evolution and tectonics of Valles Marineris wallslopes (Mars). *Geomorphology*, *37*(3–4), 329–352. https://doi.org/10.1016/S0169-555X(00)00085-4

Platz, T., & Michael, G. (2011). Eruption history of the Elysium volcanic province, Mars. *Earth and Planetary Science Letters*, *312*(1–2), 140–151. https://doi.org/10.1016/j.epsl.2011.10.001

Plesa, A.-C., Knapmeyer, M., Golombek, M. P., Breuer, D., Grott, M., Kawamura, T., et al. (2018). Present-day Mars' seismicity predicted from 3-D thermal evolution models of interior dynamics. *Geophysical Research Letters*, *45*(6), 2580–2589. https://doi.org/10.1002/2017GL076124

Plescia, J. B. (1990). Recent flood lavas in the Elysium region of Mars. *Icarus*, *88*(2), 465–490. https://doi.org/10.1016/0019-1035(90)90095-Q

Plescia, J. B. (2003). Cerberus Fossae, Elysium, Mars: A source for lava and water. *Icarus*, *164*(1), 79–95. https://doi.org/10.1016/S0019-1035(03)00139-8

Polit, A. T., Schultz, R. A., & Soliva, R. (2009). Geometry, displacement–length scaling, and extensional strain of normal faults on Mars with inferences on mechanical stratigraphy of the Martian crust. *Journal of Structural Geology*, *31*(7), 662–673. https://doi.org/10.1016/j.jsg.2009.03.016

Pollard, D. D., Delaney, P. T., Duffield, W. A., Endo, E. T., & Okamura, A. T. (1983). *Surface deformation in volcanic rift zones* (pp. 541–584). https://doi.org/10.1016/0040-1951(83)90034-3

Rivas-Dorado, S., Ruiz, J., & Romeo, I. (2021). Subsurface geometry and emplacement conditions of a giant dike system in Elysium Fossae, Mars. *Journal of Geophysical Research: Planets*, *126*(1). https://doi.org/10.1029/2020JE006512

Roberts, G. P., Matthews, B., Bristow, C., Guerrieri, L., & Vetterlein, J. (2012). Possible evidence of paleomarsquakes from fallen boulder populations, Cerberus Fossae, Mars. *Journal of Geophysical Research*, *117*(E2). https://doi.org/10.1029/2011JE003816

Rowland, J. V., Baker, E., Ebinger, C. J., Keir, D., Kidane, T., Biggs, J., et al. (2007). Fault growth at a nascent slow-spreading ridge: 2005 Dabbahu rifting episode, Afar. *Geophysical Journal International*, *171*(3), 1226–1246. https://doi.org/10.1111/j.1365-246X.2007.03584.x

Rubin, A. M. (1992). Dike-induced faulting and graben subsidence in volcanic rift zones. *Journal of Geophysical Research*, *97*(B2), 1839–1858. https://doi.org/10.1029/91JB02170

Rubin, A. M. (1995). Propagation of magma-filled cracks. *Annual Review of Earth and Planetary Sciences*, *23*(1), 287–336. https://doi.org/10.1146/annurev.ea.23.050195.001443

Rubin, A. M., & Gillard, D. (1998). Dike-induced earthquakes: Theoretical considerations. *Journal of Geophysical Research*, *103*(1), 17–30. https://doi.org/10.1029/97jb03514

Rubin, A. M., & Pollard, D. D. (1988). Dike-induced faulting in rift zones of Iceland and Afar. *Geology*, *16*(5), 413. https://doi.org/10.1130/0091-7613(1988)016<0413:difirz>2.3.co;2

Saucier, F., Humphreys, E., & Weldon, R. (1992). Stress near geometrically complex strike-slip faults: Application to the San Andreas fault at Cajon Pass, southern California. *Journal of Geophysical Research*, *97*(B4), 5081. https://doi.org/10.1029/91JB02644

Scholz, C. H. (2019). *The mechanics of earthquakes and faulting* (3rd ed.). Cambridge University Press.

Schubert, G., Solomon, S. C., Turcotte, D. L., Drake, M. J., & Sleep, N. H. (1990). Origin and thermal evolution of Mars. https://ntrs.nasa.gov/citations/19910013698

Schultz, R. A. (1989). Strike-slip faulting of ridged plains near Valles Marineris, Mars. *Nature*, *341*(6241), 424–426. https://doi.org/10.1038/341424a0

Segall, P., & Pollard, D. D. (1980). Mechanics of discontinuous faults. *Journal of Geophysical Research*, *85*(B8), 4337. https://doi.org/10.1029/JB085iB08p04337

Shaw, B. E. (2006). Initiation propagation and termination of elastodynamic ruptures associated with segmentation of faults and shaking hazard. *Journal of Geophysical Research*, *111*(B8), B08302. https://doi.org/10.1029/2005JB004093

Sibson, R. H. (1986). Rupture interaction with fault jogs. *Earthquake Source Mechanics*, *37*, 157–167. Retrieved from https://books.google.fr/books?hl=fr&lr=&id=hh1dTskgyDEC&oi=fnd&pg=PA156&dq=sibson+1986+rupture+interactions&ots=QeRawxFk2j&sig=P9Ck-FArNm1Nyy3OSRW5EHHhvPj0#v=onepage&q=sibson1986ruptureinteractions&f=false

Sigmundsson, F., Hooper, A., Hreinsdóttir, S., Vogfjörd, K. S., Ófeigsson, B. G., Heimisson, E. R., et al. (2015). Segmented lateral dyke growth in a rifting event at Bárðarbunga volcanic system, Iceland. *Nature*, *517*(7533), 191–195. https://doi.org/10.1038/nature14111

Smith, D. E., Zuber, M. T., Frey, H. V., Garvin, J. B., Head, J. W., Muhleman, D. O., et al. (2001). Mars orbiter laser altimeter: Experiment summary after the first year of global mapping of Mars, *106*(E10), 23689–23722. https://doi.org/10.1029/2000je001364

Soliva, R., & Benedicto, A. (2004). A linkage criterion for segmented normal faults. *Journal of Structural Geology*, *26*(12), 2251–2267. https://doi.org/10.1016/j.jsg.2004.06.008

Spiga, A., Banfield, D., Teanby, N. A., Forget, F., Lucas, A., Kenda, B., et al. (2018). Atmospheric science with InSight. *Space Science Reviews*, *214*(7), 109. https://doi.org/10.1007/s11214-018-0543-0

Stähler, S. C., Khan, A., Banerdt, W. B., Lognonné, P., Giardini, D., Ceylan, S., et al. (2021). Seismic detection of the Martian core. *Science*, *373*(6553), 443–448. https://doi.org/10.1126/science.abi7730

Stevanović, J., Teanby, N. A., Wookey, J., Selby, N., Daubar, I. J., Vaubaillon, J., & Garcia, R. (2017). Bolide airbursts as a seismic source for the 2018 Mars InSight mission. *Space Science Reviews*, *211*(1–4), 525–545. https://doi.org/10.1007/s11214-016-0327-3

Tanaka, K. L., Chapman, M. G., & Scott, D. H. (1992). *Geologic map of the Elysium region of Mars*. U.S. Geological Survey Geologic Investigations. Retrieved from https://pubs.er.usgs.gov/publication/i2147

Taylor, J., Teanby, N. A., & Wookey, J. (2013). Estimates of seismic activity in the Cerberus Fossae region of Mars. *Journal of Geophysical Research: Planets*, *118*(12), 2570–2581. https://doi.org/10.1002/2013JE004469

Tentler, T. (2005). Propagation of brittle failure triggered by magma in Iceland. *Tectonophysics*, *406*(1–2), 17–38. https://doi.org/10.1016/j.tecto.2005.05.016

Townsend, M. R., Pollard, D. D., & Smith, R. P. (2017). Mechanical models for dikes: A third school of thought. *Tectonophysics*, *703–704*, 98–118. https://doi.org/10.1016/j.tecto.2017.03.008

Trippanera, D., Ruch, J., Acocella, V., & Rivalta, E. (2015). Experiments of dike-induced deformation: Insights on the long-term evolution of divergent plate boundaries. *Journal of Geophysical Research: Solid Earth*, *120*(10), 6913–6942. https://doi.org/10.1002/2014JB011850

Ukawa, M., & Tsukahara, H. (1996). Earthquake swarms and dike intrusions off the east coast of Izu Peninsula, central Japan. *Tectonophysics*, *253*(3–4), 285–303. https://doi.org/10.1016/0040-1951(95)00077-1

Vaucher, J., Baratoux, D., Mangold, N., Pinet, P., Kurita, K., & Grégoire, M. (2009). The volcanic history of central Elysium Planitia: Implications for Martian magmatism. *Icarus*, *204*(2), 418–442. https://doi.org/10.1016/j.icarus.2009.06.032

Vetterlein, J., & Roberts, G. P. (2009). Postdating of flow in Athabasca Valles by faulting of the Cerberus Fossae, Elysium Planitia, Mars. *Journal of Geophysical Research*, *114*(E7), E07003. https://doi.org/10.1029/2009JE003356

Vetterlein, J., & Roberts, G. P. (2010). Structural evolution of the Northern Cerberus Fossae graben system, Elysium Planitia, Mars. *Journal of Structural Geology*, *32*(4), 394–406. https://doi.org/10.1016/j.jsg.2009.11.004

Ze, T., & Alves, T. M. (2019). Impacts of data sampling on the interpretation of normal fault propagation and segment linkage. *Tectonophysics*. https://doi.org/10.1016/j.tecto.2019.03.013

Zhang, P., Mao, F., & Slemmons, D. B. (1999). Rupture terminations and size of segment boundaries from historical earthquake ruptures in the Basin and Range Province. *Tectonophysics*, *308*(1–2), 37–52. https://doi.org/10.1016/S0040-1951(99)00089-X

References From the Supporting Information

Horvath, D.G., Moitra, P., Hamilton, C. W., Craddock, R. A., & Andrews-Hanna, J. C. (2021). Evidence for geologically recent explosive volcanism in Elysium Planitia, Mars. *Icarus*, *365*, 114499. https://doi.org/10.1016/j.icarus.2021.114499

Moitra, P., Horvath, D. G., & Andrews-Hanna, J. C. (2021). Investigating the roles of magmatic volatiles, ground ice and impact-triggering on a very recent and highly explosive volcanic eruption on Mars. *Earth and Planetary Science Letters*, *567*, 116986. https://doi.org/10.1016/j.epsl.2021.116986

Vetterlein, J., & Roberts, G. P. (2010). Structural evolution of the Northern Cerberus Fossae graben system, Elysium Planitia, Mars. *Journal of Structural Geology*, *32*, 394–406. https://doi.org/10.1016/j.jsg.2009.11.004